BNL-229826-2026-TECH

Dynamic Multipoles in the RCS

B. Podobedov

June 2026

Electron-Ion Collider

Brookhaven National Laboratory

U.S. Department of Energy

USDOE Office of Science (SC), Nuclear Physics (NP)

DISCLAIMER

Dynamic Multipoles in the RCS

Boris Podobedov, Harshita Singh

June 4, 2026

Abstract

The Rapid Cycling Synchrotron (RCS) of the Electron–Ion Collider (EIC) will accelerate polarized electrons up to 18 GeV at a repetition rate of 1 Hz. Dynamic multipoles driven by eddy currents in the vacuum chamber can affect beam dynamics and polarization preservation during the energy ramp. Building on the analytical treatment of S. Y. Lee for a ramped normal-conducting dipole magnet, we use conformal transformations to derive compact expressions for dynamic multipoles in higher-order ramped magnets with circular beam pipes. We further derive analytical frequency-domain transfer functions for both self-response and cross-response multipoles, providing compact dynamical models for their evolution during arbitrary ramp waveforms. The resulting analytical predictions are benchmarked against finite-element simulations, including the effects of practical pole geometry and beam-pipe misalignment. Finally, the expected dynamic multipoles in the RCS magnets are estimated and their implications for beam dynamics and polarization preservation are discussed.

1 Introduction

The Rapid Cycling Synchrotron (RCS) of the Electron-Ion Collider (EIC) will accelerate polarized electrons from an injection energy of 750 MeV to a top energy of up to 18 GeV with a repetition rate of 1 Hz. Careful control of both linear and nonlinear machine lattice throughout the ramp cycle is essential to avoid beam loss and preserve polarization. As such, it is important to understand, quantify, and control dynamic multipoles, primarily generated by eddy currents induced in the beam pipes passing through ramped magnets.

Even though a stainless steel circular beam pipe has been selected as the vacuum chamber, significant dynamic multipoles are expected during the RCS ramp. This is because the boundary conditions imposed by the high-permeability magnet poles break axial symmetry, resulting in strong dynamic multipoles, typically of higher order than the magnet being ramped. (Dynamic multipoles of the same order, here referred to as "self-response," are also excited and occur even in the absence of high-permeability poles. However, they are typically less harmful, as they are readily controlled with magnet power supplies.)

In addition to the magnitude of the multipoles, their time evolution is also important. To quantify this behavior in a systematic way, a complete description of the underlying dynamical system is required, for example in the form of frequency-dependent transfer functions relating the nominal magnetic fields without the beam pipe to the multipolar fields inside the pipe.

To the best of our knowledge, analytical expressions for such transfer functions have not been published. The foundational analytical treatment of this problem was given by S.Y. Lee [1], who derived the dynamic multipoles generated by a ramped dipole, although without their frequency dependence. However, corresponding analytical results for higher-order ramped magnets do not appear to be available.

While numerical methods such as finite-element modeling (FEM) can be used to compute the dynamic multipoles and their frequency response, an analytical approach offers important advantages. First, it provides explicit scaling of the response with key parameters such as beam pipe dimensions, conductivity, and magnet pole-tip radius, allowing rapid exploration of design changes. Second, it yields direct insight into the underlying physics, separating the roles of eddy currents, boundary conditions, and mode coupling. Third, it naturally produces compact dynamical models, such as transfer functions, that can be readily incorporated into beam dynamics simulations. Finally, analytical results provide a valuable benchmark for validating complicated FEM models and identifying potential inconsistencies in simulation setups.

These considerations motivate the development of an analytical framework for computing the magnitude and dynamical response of induced multipoles in ramped normal-conducting magnets, which is the focus of this paper.

At the same time, because the analytical results obtained here are new, we perform detailed benchmarking against FEM simulations for a representative quadrupole magnet design, including cases that approach the limits of the underlying theoretical assumptions. Based on this comparison, we conclude that the present theory provides a reasonably accurate description of dynamic multipoles across all relevant RCS magnet types, and we use it to make quantitative predictions for all major RCS magnets.

Importantly, at the current stage of the RCS and EIC design, significant changes to RCS magnet apertures and beam pipe dimensions remain possible. However, the analytical expressions developed here can be readily reevaluated for updated machine parameters as needed.

This paper proceeds as follows. In Section 2, we present compact expressions for the induced fields in the magnet gap of a ramped dipole magnet (with detailed derivations given in the Appendix). In Section 3, we apply conformal mapping to derive the fields due to ramped multipole magnets of arbitrary order. In Sections 4 and 5, we derive the self- and cross-response transfer functions for the magnetic multipoles. In Section 6, we present an approximate treatment of beam-pipe misalignment and evaluate the resulting dynamic dipole and other multipoles from higher-order magnets. In Section 7, we compare the analytical results with FEM simulations for a quadrupole magnet. In Section 8, we apply the results to the present RCS design parameters and obtain numerical values for the multipoles for use in beam dynamics simulations. Section 9 summarizes our conclusions.

2 Induced multipoles from a ramping dipole

Following [1], we model the dipole magnet as a pair of non-conducting, infinitely permeable parallel plates separated by a gap g, as shown in Fig. 1. In the absence of a conducting beam pipe, the time-varying magnetic field in the gap, $B_0(t)$, is assumed to be generated by the dipole main coils and to be spatially uniform and purely vertical.

The beam pipe is modeled as a thin-wall circular cylinder with radius a, wall thickness d, and conductivity σ, nominally located midway between the plates and centered at $z = 0$. Throughout this paper, the conducting circular vacuum chamber is referred to as the beam pipe. The terms "wall" and "shell" are used only when emphasizing the thin-wall boundary model, in which the induced current is represented on the conducting surface.

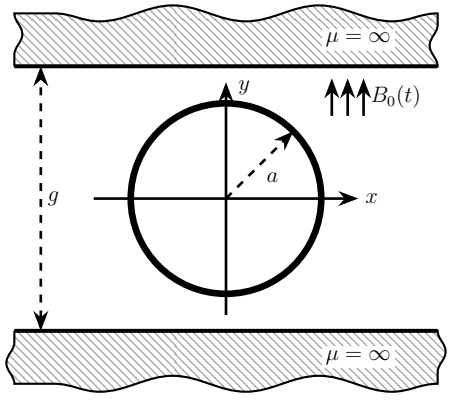

Figure 1: Dipole magnet and beam pipe model.

The problem is therefore two-dimensional, with magnetic fields confined to the transverse plane. At the timescales of interest, displacement currents can be neglected, so we remain within the quasi-magnetostatic (QMS) approximation.

We use the complex magnetic field

$$B(z) = iB_x(z) + B_y(z), \tag{2.1}$$

as a function of the complex coordinate

$$z = x + iy = re^{i\phi}. \tag{2.2}$$

The essential approximation adopted in Sections 2–3 of this paper (and relaxed later) is that proposed in Ref. [1], namely, a purely magnetostatic superposition of the field due to the main coil and that due to induced currents in the beam-pipe wall. Under this assumption, the current density in the beam-pipe wall follows from Faraday's law with only the main-coil contribution retained in the driving field:

$$J(\phi) = \sigma \dot{B}_0\, a \cos\phi. \tag{2.3}$$

With this approximation, the problem of induced multipoles inside the beam pipe becomes easily tractable. For an arbitrary beam-pipe cross-section, the resulting solution was obtained in Ref. [1] by the method of images and expressed as infinite series whose multipole coefficients are given by integrals over the cross-section.

For later use, it is convenient to have a compact closed-form expression for the induced field in a circular beam pipe. In the Appendix, we derive such an expression using a well-known Green's function. The result is expressed in terms of the free-space dipolar field penetration time constant

$$\bar{\tau}_0 = \frac{1}{2}\mu_0 \sigma d a, \tag{2.4}$$

and the normalized variables

$$\hat{z} = \frac{z}{a}, \qquad \hat{g} = \frac{g}{a}. \tag{2.5}$$

The field inside the pipe is

$$B(\hat{z}) = -\bar{\tau}_0 \dot{B}_0 \left(1 + \frac{1}{\hat{z}^2} - \frac{\pi^2}{\hat{g}^2}\,\mathrm{csch}^2\!\left(\frac{\pi\hat{z}}{\hat{g}}\right)\right), \qquad |\hat{z}| < 1, \tag{2.6}$$

whereas outside the pipe,

$$B(\hat{z}) = -\bar{\tau}_0 \dot{B}_0 \left(-\frac{\pi^2}{\hat{g}^2}\,\mathrm{csch}^2\!\left(\frac{\pi\hat{z}}{\hat{g}}\right)\right), \qquad |\hat{z}| > 1, \qquad |\Im(\hat{z})| < \frac{\hat{g}}{2}. \tag{2.7}$$

These expressions satisfy the required boundary conditions at the beam-pipe wall,

$$\big(B(\hat{z})\big)^{+} - \big(B(\hat{z})\big)^{-} = -\mu_0 d\, J(\phi)\, e^{-i\phi} = -\mu_0 \sigma d a\, \dot{B}_0\, e^{-i\phi}\cos\phi, \qquad \hat{z} = e^{i\phi}, \quad |\hat{z}| = 1, \tag{2.8}$$

where + and - refer to the two sides of the thin shell, and at the magnet poles,

$$\Im\left(B\left(x \pm i\frac{\hat{g}}{2}\right)\right) = 0, \qquad x \in \mathbb{R}. \tag{2.9}$$

A less compact, but mathematically equivalent, form of Eq. (2.6) was derived in Ref. [2].

Expanding Eq. (2.6) near $\hat{z} = 0$, we obtain

$$B(\hat{z}) = -\bar{\tau}_0 \dot{B}_0 \left(1 + \frac{\pi^2}{3\hat{g}^2} - \frac{\pi^4\hat{z}^2}{15\hat{g}^4} + \frac{2\pi^6\hat{z}^4}{189\hat{g}^6} - \frac{\pi^8\hat{z}^6}{675\hat{g}^8} + \frac{2\pi^{10}\hat{z}^8}{10395\hat{g}^{10}} - \frac{1382\pi^{12}\hat{z}^{10}}{58046625\hat{g}^{12}} + O\big(\hat{z}^{12}\big)\right), \tag{2.10}$$

where the leading term is the dynamic dipole; its negative sign is consistent with Lenz's law. The $\hat{z}^2$, $\hat{z}^4$, ... terms correspond to the dynamic sextupole, dynamic decapole, and so on. By symmetry, only multipoles proportional to even powers of $\hat{z}$ are allowed.

One may verify that the multipole coefficients from Eq. (2.10) are consistent with those obtained by applying the general formalism of Ref. [1] to the case of a circular beam pipe.

3 Conformal mapping

We have derived compact expressions for the fields produced by a ramped dipole between infinitely permeable parallel plates. We now use conformal mapping to extend these results to ramped multipole magnets of arbitrary order with infinitely permeable poles of ideal shape.

The results below depend on the precise definition of the multipole coefficients. In this paper, the normal (b_n) and skew (a_n) multipoles are defined by

$$B(z) = \sum_{n=1}^{\infty} n\big(b_n + i a_n\big) z^{n-1}, \tag{3.1}$$

or, in normalized variables,

$$B(\hat{z}) = \sum_{n=1}^{\infty} n\big(\hat{b}_n + i \hat{a}_n\big) \hat{z}^{n-1}. \tag{3.2}$$

With this convention, the indices $n = 1, 2, 3, \ldots$ correspond to the dipole, quadrupole, sextupole, and so on. This indexing differs from that used in Ref. [1].

We begin with the quadrupole case and denote its complex field by $B_Q(\hat{z})$. Introduce the conformal map

$$\hat{w} = \hat{z}^2, \tag{3.3}$$

where $\hat{z}$ denotes the normalized coordinate in the quadrupole geometry and $\hat{w}$ the corresponding coordinate in the dipole geometry. This map sends the unit circle, representing the beam pipe, onto itself. At the same time, the dipole pole boundaries

$$\Im(\hat{w}) = \pm\frac{\hat{g}}{2} \tag{3.4}$$

are mapped into the hyperbolas

$$\hat{y}_{\text{p.s.}}(\hat{x}) = \pm\frac{\hat{r}_p^2}{2\hat{x}}, \tag{3.5}$$

which are the pole surfaces of an ideal quadrupole with normalized pole-tip radius

$$\hat{r}_p \equiv \frac{r_p}{a} = \sqrt{\frac{\hat{g}}{2}}. \tag{3.6}$$

The field transforms according to

$$B_Q(\hat{z}) = \frac{1}{2}\frac{d\hat{w}}{d\hat{z}}\, B_D(\hat{w})\Big|_{\hat{w}\to\hat{z}^2} = \hat{z}\, B_D\big(\hat{z}^2\big)\,, \tag{3.7}$$

where the factor $1/2$ is included so that the transformed field satisfies the correct thin-shell boundary condition on the beam-pipe wall,

$$\big(B_Q(\hat{z})\big)^+ - \big(B_Q(\hat{z})\big)^- = -\mu_0 d\, J(\phi)\, e^{-i\phi} = -\mu_0 \sigma d a^2\, \dot{\hat{b}}_2^{(e)}\, e^{-i\phi} \cos 2\phi, \qquad \hat{z} = e^{i\phi}, \quad |\hat{z}| = 1. \tag{3.8}$$

Here $\dot{\hat{b}}_2^{(e)}$ denotes the time derivative of the externally applied quadrupole coefficient, with the superscript (e) indicating that only the main-coil contribution is retained in Faraday's law, as in Eq. (2.8).

The extra factor $1/2$ in Eq. (3.7) is needed because the conformal map preserves harmonic solutions and maps the dipole pole boundaries to the quadrupole geometry, but does not preserve the dynamic thin-shell boundary condition on the conducting beam-pipe wall. In general, conformal maps rescale lengths by the local factor $|d\hat{w}/d\hat{z}|$, so boundary conditions involving field jumps and wall currents are not invariant. For the present circular beam pipe, however, the map $\hat{w} = \hat{z}^2$ has $|d\hat{w}/d\hat{z}| = 2$ on $|\hat{z}| = 1$, i.e. a constant scale factor along the wall, so the resulting boundary-condition mismatch can be removed by a single global factor $1/2$.

Substituting the dipolar-drive fields from Eqs. (2.6)–(2.7) into Eq. (3.7), we obtain, inside the beam pipe,

$$B_Q(\hat{z}) = -\frac{1}{2}\bar{\tau}_0\, \dot{\hat{b}}_2^{(e)} \left(2\hat{z} + \frac{2}{\hat{z}^3} - \frac{\pi^2 \hat{z}}{2\hat{r}_p^4}\, \operatorname{csch}^2\!\left(\frac{\pi \hat{z}^2}{2\hat{r}_p^2}\right)\right), \qquad |\hat{z}| < 1, \tag{3.9}$$

whereas outside the pipe,

$$B_Q(\hat{z}) = -\frac{1}{2}\bar{\tau}_0\,\dot{\hat{b}}_2^{(e)}\left(-\frac{\pi^2\hat{z}}{2\hat{r}_p^4}\,\mathrm{csch}^2\!\left(\frac{\pi\hat{z}^2}{2\hat{r}_p^2}\right)\right), \qquad |\hat{z}|>1, \qquad \left|\Im(\hat{z}^2)\right| < \frac{\hat{g}}{2}. \tag{3.10}$$

One may verify directly that the tangential component of the field vanishes on the pole surfaces, as required for $\mu \to \infty$.

The fields due to a ramped multipole magnet of arbitrary order n with ideal pole shapes follow in exact analogy with the quadrupole case, using the conformal map

$$\hat{w} = \hat{z}^n, \tag{3.11}$$

where $\hat{z}$ denotes the normalized coordinate in the n-pole geometry and $\hat{w}$ the corresponding coordinate in the dipole geometry. This map sends the unit circle onto itself and transforms the dipole pole boundaries

$$\Im(\hat{w}) = \pm\frac{\hat{g}}{2} \tag{3.12}$$

into the pole surfaces of an ideal n-pole magnet. The corresponding normalized pole-tip radius is

$$\hat{r}_p = \left(\frac{\hat{g}}{2}\right)^{1/n}. \tag{3.13}$$

The complex field transforms as

$$B_n(\hat{z}) = \frac{1}{n}\frac{d\hat{w}}{d\hat{z}}\,B_D(\hat{w})\Big|_{\hat{w}\to\hat{z}^n} = \hat{z}^{\,n-1}B_D(\hat{z}^n)\,, \tag{3.14}$$

where, as in the quadrupole case, the factor $1/n$ is included so that the transformed field satisfies the correct thin-shell boundary condition on the beam-pipe wall, given by

$$\big(B_n(\hat{z})\big)^+ - \big(B_n(\hat{z})\big)^- = -\mu_0 d\,J_n(\phi)\,e^{-i\phi} = -\mu_0\sigma d a^n\,\dot{\hat{b}}_n^{(e)}\,e^{-i\phi}\cos(n\phi), \qquad \hat{z}=e^{i\phi}, \quad |\hat{z}|=1. \tag{3.15}$$

The final result is, inside the pipe,

$$B_n(\hat{z}) = -\bar{\tau}_0\,\dot{\hat{b}}_n^{(e)}\left(\hat{z}^{n-1} + \frac{1}{\hat{z}^{n+1}} - \frac{\pi^2\hat{z}^{n-1}}{4\hat{r}_p^{2n}}\,\mathrm{csch}^2\!\left(\frac{\pi\hat{z}^n}{2\hat{r}_p^n}\right)\right), \qquad |\hat{z}|<1, \tag{3.16}$$

where $\dot{\hat{b}}_n^{(e)}$ denotes the time derivative of the externally applied normal n-pole coefficient.

Outside the pipe,

$$B_n(\hat{z}) = -\bar{\tau}_0\,\dot{\hat{b}}_n^{(e)}\left(-\frac{\pi^2\hat{z}^{n-1}}{4\hat{r}_p^{2n}}\,\mathrm{csch}^2\!\left(\frac{\pi\hat{z}^n}{2\hat{r}_p^n}\right)\right), \qquad |\hat{z}|>1, \qquad |\Im(\hat{z}^n)| < \hat{r}_p^n. \tag{3.17}$$

For $n=1$, these expressions recover the dipole formulas derived earlier, Eqs. (2.6)–(2.7), provided one takes $\hat{r}_p = \hat{g}/2$.

For a pure skew n-pole excitation, the corresponding fields are obtained by replacing $\dot{\hat{b}}_n^{(e)}$ with $i\,\dot{\hat{a}}_n^{(e)}$.

For later use, we record the expansions of the quadrupole and sextupole fields near the center of the pipe:

$$B_Q(\hat{z}) = -\bar{\tau}_0\,\dot{\hat{b}}_2^{(e)}\left(\left[1+\frac{\pi^2}{12\hat{r}_p^4}\right]\hat{z} - \frac{\pi^4}{240\hat{r}_p^8}\hat{z}^5 + \frac{\pi^6}{6048\hat{r}_p^{12}}\hat{z}^9 - \frac{\pi^8}{172800\hat{r}_p^{16}}\hat{z}^{13} + O\big(\hat{z}^{17}\big)\right), \tag{3.18}$$

and

$$B_S(\hat{z}) = -\bar{\tau}_0\,\dot{\hat{b}}_3^{(e)}\left(\left[1+\frac{\pi^2}{12\hat{r}_p^6}\right]\hat{z}^2 - \frac{\pi^4}{240\hat{r}_p^{12}}\hat{z}^8 + \frac{\pi^6}{6048\hat{r}_p^{18}}\hat{z}^{14} - \frac{\pi^8}{172800\hat{r}_p^{24}}\hat{z}^{20} + O\big(\hat{z}^{26}\big)\right). \tag{3.19}$$

These examples illustrate a general pattern: the expansion for a driving multipole of order n contains only powers $\hat{z}^{(2k+1)n-1}$, $k=0,1,\ldots$, with coefficients that are independent of n and repeat across all multipole orders.

This structure allows a closed-form representation of the near-axis field:

$$\begin{aligned} B_n(\hat{z}) &= -\bar{\tau}_0\,\dot{\hat{b}}_n^{(e)}\left[\left(1+\frac{c_0}{\hat{r}_p^{2n}}\right)\hat{z}^{n-1}+\sum_{k=1}^{\infty}c_k\,\frac{\hat{z}^{(2k+1)n-1}}{\hat{r}_p^{(2k+2)n}}\right] \\ &= -\bar{\tau}_0\,\dot{\hat{b}}_n^{(e)}\left(1+\frac{c_0}{\hat{r}_p^{2n}}\right)\hat{z}^{n-1}+\sum_{k=1}^{\infty}(2k+1)n\,\tau_{(2k+1)n,n}\,\dot{\hat{b}}_n^{(e)}\,\hat{z}^{(2k+1)n-1}. \end{aligned} \tag{3.20}$$

The universal coefficients are

$$c_k = \frac{(2k+1)\mathbb{B}_{2k+2}}{(2k+2)!}\,\pi^{2k+2}, \qquad k=0,1,\ldots, \tag{3.21}$$

where $\mathbb{B}_{2k+2}$ are Bernoulli numbers (e.g., $\mathbb{B}_2=\frac{1}{6}$, $\mathbb{B}_4=-\frac{1}{30}$, $\mathbb{B}_6=\frac{1}{42}$).

For $k\geq 1$, the corresponding cross-term time constants are defined as

$$\tau_{m,n} \equiv \frac{1}{\dot{\hat{b}}_n^{(e)}}\frac{1}{m!}\,\frac{d^{m-1}}{d\hat{z}^{m-1}}B_n(\hat{z})\bigg|_{\hat{z}=0}, \tag{3.22}$$

which gives

$$\tau_{m,n} = -\frac{\bar{\tau}_0}{m}\,\frac{(m/n)\mathbb{B}_{m/n+1}}{(m/n+1)!}\,\frac{\pi^{m/n+1}}{\hat{r}_p^{m+n}}, \qquad \frac{m}{n}=3,5,7,\ldots. \tag{3.23}$$

The induced fields given by Eqs. (3.16)–(3.17) for the three lowest driving multipoles, for $\hat{r}_p=1.2$, are shown in the top row of Fig. 2. As expected, the n-pole field structure (self-response $\propto \hat{z}^{n-1}$) dominates inside the beam pipe. The bottom row shows the same fields with the self-response term subtracted, revealing the cross-response contributions. In agreement with Eq. (3.20), only multipole orders satisfying the selection rule $n\to(2k+1)n$ are present, and the lowest-order cross term dominates over all higher-order contributions. These dynamic cross-terms therefore follow the same systematic-multipole sequence expected from the symmetry of an ideal n-pole magnet [3]. Their rapid decrease with multipole order reflects the fast convergence of the series in Eq. (3.20).

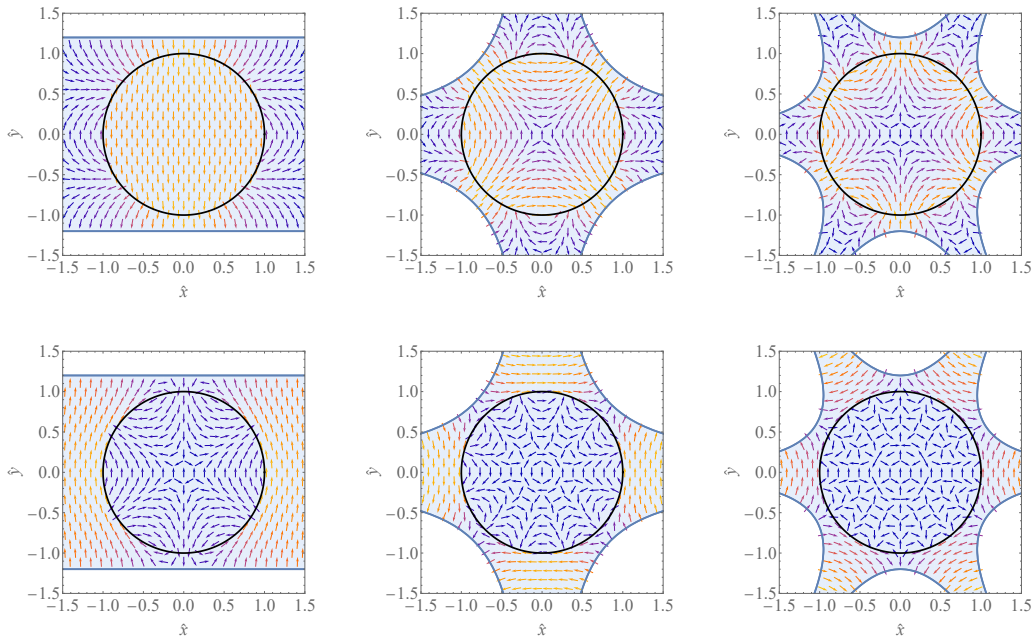

Figure 2: (top) Induced fields, $B_n(\hat{z})/(\bar{\tau}_0\,\dot{\hat{b}}_n^{(e)})$, for $n=1,2,3$ for $\hat{r}_p=1.2$; (bottom) same with leading term $\propto \hat{z}^{n-1}$ (self-response) subtracted.

4 Magnetic multipole transfer functions: self-response

In the previous sections, the induced magnetic field was written as a function of the transverse complex coordinate z, while the time dependence entered only parametrically through the time derivatives of the external driving multipole coefficients. In this section, we make the time dependence explicit in order to pass from field expressions with parametric time dependence to a dynamical description in terms of transfer functions. For compactness, instead of working with the full space- and time-dependent field $B(z,t)$, we use the time-dependent multipole coefficients $b_m(t)$ and $a_m(t)$, with the z-dependence understood from Eq. (3.1).

We then pass to the Laplace domain, with transform variable p; the frequency response is obtained by evaluating the transfer function at $p = i\omega$. We define the transfer functions in matrix form as

$$H_{m,n}(p) \equiv \frac{b_m^{(i)}(p)}{b_n^{(e)}(p)} = a^{n-m}\frac{\hat{b}_m^{(i)}(p)}{\hat{b}_n^{(e)}(p)}, \tag{4.1}$$

where m denotes the multipole order observed inside the pipe and n the externally driven multipole order. The superscript (i) denotes the total internal field seen by the beam, while (e) denotes the externally applied drive field that would be present in the absence of the conducting pipe; it should not be interpreted as the field exterior to the pipe wall.

The transfer functions for the skew multipoles (more generally skew-to-skew, skew-to-normal, and normal-to-skew) are defined analogously. In what follows, however, we restrict attention to the normal multipoles; the extension to the skew case is straightforward.

In the absence of magnet poles, i.e. in the free-space limit, these transfer functions are given by [5, 6]

$$H_{m,m}(p) = \frac{1}{1 + p\bar{\tau}_0/m}, \qquad r_p/a \to \infty, \tag{4.2}$$

while the cross-response vanishes by symmetry,

$$H_{m,n}(p) = 0, \qquad m \neq n, \qquad r_p/a \to \infty. \tag{4.3}$$

We now consider the case with magnet poles, starting with the dipole drive,

$$b_1^{(e)}(t) = B_0(t). \tag{4.4}$$

From the near-axis expansion of the dipole field, Eq. (2.10), the dipole component inside the pipe is

$$b_1^{(i)}(t) = b_1^{(e)}(t) - \tau_1\, \dot{b}_1^{(e)}(t), \tag{4.5}$$

where

$$\tau_1 \equiv \bar{\tau}_0 \left(1 + \frac{\pi^2 a^2}{3g^2}\right) \tag{4.6}$$

is the effective dipolar response time, including the increase due to the high-permeability pole boundaries.

Passing to the Laplace domain, and assuming zero initial conditions, gives

$$\frac{b_1^{(i)}(p)}{b_1^{(e)}(p)} = 1 - p\tau_1. \tag{4.7}$$

This expression is not itself the transfer function, but only the first two terms of its expansion about $p = 0$; by itself, it does not obey causality.

A useful heuristic derivation of the corresponding causal approximation is obtained by viewing the response as repeated coupling between the field on the pipe wall and the induced wall current. In the thin-wall QMS limit, each induced dipole correction is proportional to p, so the first one may be written as

$$b_{1,\mathrm{ind}}^{(1)}(p) = -\,p\,\tau_1\, b_1^{(e)}(p). \tag{4.8}$$

If this induced dipole field is then treated as an additional drive acting on the wall, the same linear relation applies at each subsequent step, provided all other modes are neglected. One then obtains

$$b_{1,\mathrm{ind}}^{(j)}(p) = (-p\tau_1)^j\, b_1^{(e)}(p), \qquad j \geq 1. \tag{4.9}$$

Summing the external drive and all induced contributions gives

$$b_1^{(i)}(p) = b_1^{(e)}(p) + \sum_{j\geq 1} b_{1,\mathrm{ind}}^{(j)}(p) \tag{4.10}$$

$$= b_1^{(e)}(p) \left[1 + \sum_{j\geq 1} (-p\tau_1)^j\right], \tag{4.11}$$

and hence the single-pole approximation

$$H_{1,1}(p) \equiv \frac{b_1^{(i)}(p)}{b_1^{(e)}(p)} = \frac{1}{1+p\tau_1}. \tag{4.12}$$

Importantly, in this formulation, the pipe boundary condition is treated self-consistently within the retained dipole mode, in contrast to the earlier approximation, Eq. (3.8), where the wall current was computed from the main-coil field alone.

In the limit $g \gg a$, Eq. (4.12) reduces to the free-space result, Eq. (4.2). For any $g > 2a$, its low-frequency expansion agrees with Eq. (4.7).

Equation (4.12) should be understood as a single-mode approximation. As is evident from the multipole expansion in Eq. (2.10), a ramped dipole excites not only the dipole component, but also higher-order multipoles. These higher modes, in turn, feed back into the dipole response. Once this inter-mode coupling is retained, the transfer function is no longer strictly single-pole.

Nevertheless, as discussed below, the simple single-pole form in Eq. (4.12) remains useful even though the exact thin-wall response contains inter-mode coupling. The purpose of the following discussion is therefore to establish the range of validity of Eq. (4.12), rather than to replace it.

A more complete derivation, omitted here, may be constructed by retaining the lowest N modes allowed by symmetry. For $N = 2$, one finds, for example,

$$H_{1,1}^{(N=2)}(p) = \frac{1+p\tau_{3,3}}{(1+p\tau_1)(1+p\tau_{3,3}) - p^2\tau_{1,3}\tau_{3,1}}. \tag{4.13}$$

Here $\tau_{3,3}$, $\tau_{1,3}$, and $\tau_{3,1}$ are positive, p-independent constants. In the free-space limit $g/a \to \infty$, one has $\tau_{3,3} \to \bar{\tau}_0/3$, while $\tau_{1,3}$ and $\tau_{3,1}$ tend to zero.

This more general treatment shows that:

- the N-mode transfer function is N-th order, with N poles and $N-1$ zeros;
- the dominant pole generally differs from $-1/\tau_1$ predicted by the single-pole approximation, Eq. (4.12);
- for any N, the $\{0,1\}$ Padé approximation of the N-mode transfer function about $p = 0$ is identical to Eq. (4.12);
- as N increases, the magnitude and phase responses of the N-mode transfer functions rapidly approach those of Eq. (4.12) over an expanding frequency range, approximately $|p| \lesssim (2N-1)/\tau_1$.

Equation (4.12) therefore has intrinsic value: although not exact except in the free-space limit, it is the correct lowest-order physical Padé approximation to the dipole self-response about $p = 0$, and it also provides an accurate representation over a finite frequency range. Moreover, the last bullet suggests that, within the thin-shell model, this range expands without bound as $N \to \infty$, so that the only ultimate limitation comes from the breakdown of the thin-shell approximation itself. This breakdown occurs when the skin depth becomes comparable to the wall thickness, corresponding to frequencies of order $|p_{\max}| \sim 2/(\mu_0\sigma d^2)$.

The approach above that led to the single-pole dipole transfer-function approximation, Eq. (4.12), extends directly to a drive multipole of arbitrary order m. From the leading term of the near-axis expansion of the general field expression, Eq. (3.16), one obtains the self-response transfer function

$$H_{m,m}(p) \equiv \frac{b_m^{(i)}(p)}{b_m^{(e)}(p)} = \frac{1}{1+p\tau_m}, \tag{4.14}$$

with

$$\tau_m = \frac{\bar{\tau}_0}{m}\left(1+\frac{\pi^2}{12}\left(\frac{a}{r_p}\right)^{2m}\right). \tag{4.15}$$

For $m = 1$, one has $r_p = g/2$, so that τ_m agrees with τ_1 defined in Eq. (4.6). For $m = 2$ and $m = 3$, Eq. (4.15) is likewise consistent with the explicit near-axis expansions in Eqs. (3.18) and (3.19). Finally, for any m, Eqs. (4.14) and (4.15) correctly reproduce Eq. (4.2) in the free-space limit.

For finite r_p/a, Eq. (4.14) should be understood as the lowest-order physical Padé approximation to the exact self-response transfer function near $p = 0$. More importantly, it also provides an accurate approximation to the true transfer function over the frequency range $|p| \lesssim 2/(\mu_0\sigma d^2)$.

In typical accelerator magnets, the pole-tip radius is only slightly larger than the pipe radius, so that $a/r_p \approx 1$. Eqs. (4.14) and (4.15) then show that the high-permeability poles increase the fundamental response time constant by approximately $\pi^2/12 \approx 80\%$, nearly independently of the multipole order m. Equivalently, the induced self-response field is larger by the same factor. Both statements reflect the same physical effect: at frequencies $\omega \gg m/\bar{\tau}_0$, time-varying external fields are attenuated inside the beam pipe by about a factor of 1.8 more strongly than in the absence of high-permeability magnet poles.

Before proceeding to the cross-response transfer functions, we emphasize a convention used throughout this paper. All transfer functions are defined for the total multipole component of the magnetic field seen by the beam inside the pipe. For a self-response, this total field includes the externally driven multipole itself, and therefore the self-response transfer function has unit gain at zero frequency. Thus, for an n-pole drive,

$$H_{n,n}(p) = \frac{1}{1+p\tau_n}, \tag{4.16}$$

whereas the transfer function for the induced part of the self-response alone would be

$$H_{n,n}^{(\mathrm{ind})}(p) = H_{n,n}(p) - 1 = -\frac{p\tau_n}{1+p\tau_n}. \tag{4.17}$$

The latter quantity is useful only when explicitly separating the induced field from the externally applied field; otherwise $H_{n,n}(p)$ always denotes the total internal self-response.

5 Magnetic multipole transfer functions: cross-term response

We now consider cross-term transfer functions $H_{m,n}(p)$ with $m \neq n$, where a driving multipole of order n generates a response of order m inside the pipe. As follows from the expansion of the induced fields in Section 3, see Eqs. (3.20) and (3.23), only multipole orders satisfying $m/n = 3, 5, 7, \ldots$ result in a nonzero cross-response.

Let $B_n(\hat{z})$ denote the induced field inside the pipe due to a ramped multipole of order n, as derived in Section 3. Unlike the self-response case, the externally applied drive field contains no m-pole component; the m-pole response arises entirely from currents induced in the beam-pipe wall. Consequently, the low-frequency behavior of the cross-response must scale as $H_{m,n}(p) \propto p$.

This response can be obtained directly from the induced field expressions in Eq. (3.16) by passing to the Laplace domain via the substitution

$$\dot{\hat{b}}_n^{(e)} \to p\,\hat{b}_n^{(e)}(p), \tag{5.1}$$

and using the definition of $\tau_{m,n}$ given in Eqs. (3.22)–(3.23).

The leading-order contribution is then given by

$$H_{m,n}(p) = a^{n-m}p\tau_{m,n} + O(p^2), \qquad \frac{m}{n} = 3, 5, 7, \ldots. \tag{5.2}$$

For instance, the leading quadrupole-induced higher multipole, the dodecapole, follows from Eqs. (3.22)–(3.23),

$$b_6^{(i)}(p) = H_{6,2}(p) b_2^{(e)}(p), \tag{5.3}$$

with

$$H_{6,2}(p) = a^{-4}\, p\bar{\tau}_0\, \frac{1}{6}\frac{\pi^4}{240\hat{r}_p^8} + O(p^2) = p\bar{\tau}_0\, \frac{\pi^4 a^4}{1440 r_p^8} + O(p^2). \tag{5.4}$$

The same result can also be read off directly from the field expansion in Eq. (3.18).

At higher frequencies, the low-frequency scaling $H_{m,n}(p) \propto p$ must break down. Even if the skin effect is neglected (which is exact for an infinitely thin beam-pipe wall), the cross-term transfer function must vanish as $p \to \infty$. Physically, this reflects the fact that time-varying external fields are increasingly screened by the induced currents, so that the field inside the pipe is strongly attenuated. Furthermore, as follows from the thin-wall boundary condition, cross-term and self-response transfer functions must have the same high-frequency scaling, $H_{m\neq n,n}(p) \sim H_{n,n}(p) \sim 1/p$.

These considerations suggest a minimal causal form

$$H_{m,n}(p) = a^{n-m} \frac{p\,\tau_{m,n}}{(1+p\tau_{m,n}^{(1)})(1+p\tau_{m,n}^{(2)})}, \qquad \frac{m}{n} = 3, 5, 7, \ldots, \tag{5.5}$$

with $\tau_{m,n}^{(1)}$ and $\tau_{m,n}^{(2)}$ representing characteristic time constants of the cross-response. Approximating these by the self-response time scales of the participating modes defined in Eq. (4.15) yields

$$H_{m,n}(p) = a^{n-m} \frac{p\,\tau_{m,n}}{(1+p\tau_m)(1+p\tau_n)}, \qquad \frac{m}{n} = 3, 5, 7, \ldots. \tag{5.6}$$

6 Dynamic multipoles due to misaligned beam pipe

The results of the previous sections show that a ramped external drive $\hat{b}_n^{(e)}(t)$ induces not only the response of the same multipole order (the "self-response"), but also higher-order multipoles of orders $3n, 5n, \ldots$. Importantly, no multipole of order lower than n is excited for a circular beam pipe centered on the magnet symmetry center. By contrast, in a related problem studied for the ESR vacuum chamber, which lacks axial symmetry but retains two mid-plane symmetries, lower-order multipoles were found to be excited; in particular, a ramped sextupole generates a dynamic dipole [4].

The absence of a dynamic dipole from ramped higher-order magnets is generally favorable for the RCS, due to its enhanced sensitivity to dipole errors from any source. In practice, however, the beam pipe will inevitably be misaligned with respect to the magnet center. Such a misalignment breaks the axial symmetry of the pipe boundary condition and, in general, allows multipoles of arbitrary order to be generated, including a dynamic dipole.

For the small misalignments expected in practice, these additional multipoles should remain small compared with the symmetry-allowed terms derived in the previous sections. Nevertheless, because the dynamic dipole, and potentially other low-order multipoles, are particularly important for the RCS, here we derive them approximately in the presence of small beam-pipe misalignment. We focus on multipoles generated by ramped higher-order magnets, since the dipolar-drive results for the displaced pipe are already included in Eqs. (A.17)–(A.19).

Note that, for the offset pipe, direct application of conformal maps to the dipole expressions does not readily yield the fields due to higher-order ramped magnets. The map $\hat{w} = \hat{z}^n$ transforms the displaced circular pipe into a non-circular cross-section, while a map centered at the offset pipe, $\hat{w} = (\hat{z} - \hat{\delta}_x - i\hat{\delta}_y)^n$, produces higher-order magnets aligned with the transformed pipe. Both geometries are qualitatively different from the displaced circular pipe in a multipole magnet. Another approach is to derive the field in the dipole plane in the presence of the pipe "pre-image," which maps to a properly offset circular pipe in the multipole magnet (for example, a Cassini oval in the quadrupole case). However, unlike the centered-pipe case, the boundary conditions on this pre-image are not preserved under conformal transformation (see discussion after Eq. (3.8)).

Instead, we start from the free-space asymptotic. Consider a beam pipe offset horizontally by $\delta_z = \delta_x + i0$ with respect to the center of the externally applied quadrupole field. By linearity, the pipe is subjected to

the sum of a quadrupole field, $2b_2^{(e)}z$, and a dipole field, $2\delta_x b_2^{(e)}$. The corresponding multipole components inside the pipe, $b_2^{(i)}$ and $b_1^{(i)}$, follow from the transfer functions, Eq. (4.2). Transforming the quadrupole component to $z = 0$ (shift by $-\delta_x$) yields the transfer function for a horizontally displaced pipe

$$H_{1,2}(p;\delta_x) = \frac{1}{b_2^{(e)}}\left(\frac{2\delta_x b_2^{(e)}}{1+p\bar{\tau}_0} - \frac{2\delta_x b_2^{(e)}}{1+p\bar{\tau}_0/2}\right) = -\delta_x \frac{p\bar{\tau}_0}{(1+p\bar{\tau}_0)(1+p\bar{\tau}_0/2)}, \qquad r_p/a \to \infty. \tag{6.1}$$

The sextupole-induced dipole for a shifted pipe can be obtained similarly (accounting for sextupole and quadrupole feeddowns):

$$H_{1,3}(p;\delta_x) = -\delta_x^2 \frac{p\bar{\tau}_0}{(1+p\bar{\tau}_0)(1+p\bar{\tau}_0/2)(1+p\bar{\tau}_0/3)}, \qquad r_p/a \to \infty. \tag{6.2}$$

Transfer functions for dipole response driven by higher-order multipoles satisfy $H_{1,n}(p;\delta_x) \propto \delta_x^{n-1}$.

For the case with magnet poles, rather than carrying out a rigorous derivation, we conjecture that replacing, in the derivation above, each free-space mode time constant with its "with-poles" value from Eq. (4.15), $\bar{\tau}_0/m \to \tau_m$, provides a useful approximation for $r_p \gtrsim a$.

In this manner, the quadrupole-induced dipole, $b_1^{(i)} = H_{1,2}(p;\delta_x)b_2^{(e)}$, can be estimated as

$$H_{1,2}(p;\delta_x) = -2\delta_x \frac{p(\tau_1-\tau_2)}{(1+p\tau_1)(1+p\tau_2)}. \tag{6.3}$$

Dipole components induced by higher-order time-varying magnets scale with higher powers of δ_x and can normally be neglected.

With the replacement $\delta_x \to i\delta_y$, Eqs. (6.1) and (6.3) apply to the case of a vertically offset pipe; for these cases, the resulting dipole should be interpreted as skew rather than normal. In contrast, for vertical offset, Eq. (6.2) produces a normal dipole, with sign change.

The estimate above is the simplest example of a more general geometric-feeddown construction, which we now describe. To obtain the low-frequency $O(\delta_x)$ displaced-pipe transfer functions, we account for two distinct geometric effects. First, when the externally applied n-pole field is expressed in coordinates centered on the displaced pipe, it feeds down to lower-order drive multipoles. Second, after the pipe-centered response is computed, the resulting internal field must be transformed back to the magnet-centered coordinate system, producing feeddown of the induced multipoles. In what follows we retain these geometric feeddown effects, while neglecting additional $O(\delta_x)$ corrections that could arise directly from the magnet pole boundary conditions. Support for this approximation comes from comparing the displaced-pipe expansions of the dipolar fields for horizontal and vertical offsets, Eqs. (A.18) and (A.20), where the magnitudes of the $O(\delta)$ coefficients are found to be quite similar. Since, in the dipole problem, the pole boundary conditions affect only the vertical displacement case (horizontal displacement is unaffected because of translational symmetry), this suggests that any direct pole-boundary contributions to the $O(\delta)$ feeddown terms should be small or absent for higher-order drive multipoles as well.

Let u denote the coordinate centered on the displaced pipe and z the coordinate centered on the magnet, with

$$z = u + \delta_x. \tag{6.4}$$

A pure external n-pole in the magnet-centered frame is

$$B^{(e)}(z) = nb_n^{(e)}z^{n-1}. \tag{6.5}$$

In the pipe-centered coordinate system this becomes, to first order in δ_x,

$$B^{(e)}(u) = nb_n^{(e)}(u+\delta_x)^{n-1} = nb_n^{(e)}u^{n-1} + n(n-1)\delta_x b_n^{(e)}u^{n-2} + O(\delta_x^2). \tag{6.6}$$

Using the multipole convention of Eq. (3.1), this corresponds to the local drive coefficients

$$b_n^{(e,\mathrm{loc})} = b_n^{(e)}, \qquad b_{n-1}^{(e,\mathrm{loc})} = n\delta_x b_n^{(e)} \tag{6.7}$$

at $O(\delta_x)$.

Let $H_{m,n}(p)$ denote the centered-pipe transfer function derived in the previous sections, including the total self-response when $m = n$ and the induced cross-response when $m \neq n$. In the following expressions, centered-pipe transfer functions that are either undefined or forbidden by symmetry are to be set to zero.

The internal pipe-centered response is then

$$b_m^{(i,\mathrm{loc})} = H_{m,n}(p) b_n^{(e)} + n\delta_x H_{m,n-1}(p) b_n^{(e)} + O(\delta_x^2). \tag{6.8}$$

The first term is the response to the original n-pole drive, while the second term is the response to the local $(n-1)$-pole feeddown of the externally applied field.

Transforming the internal field back to the magnet-centered coordinate, $u = z - \delta_x$, gives

$$b_m^{(i)} = b_m^{(i,\mathrm{loc})} - (m+1)\delta_x b_{m+1}^{(i,\mathrm{loc})} + O(\delta_x^2). \tag{6.9}$$

Keeping only terms linear in δ_x, the displacement-induced correction to the centered-pipe transfer function is, for any observed multipole order $m \geq 1$,

$$H_{m,n}(p;\delta_x) = \delta_x \left[n H_{m,n-1}(p) - (m+1) H_{m+1,n}(p) \right]. \tag{6.10}$$

Here $H_{m,n}(p;\delta_x)$ denotes only the $O(\delta_x)$ contribution generated by the horizontal displacement. Centered-pipe transfer functions that are either undefined or forbidden by symmetry are set to zero; equivalently, the two terms on the right-hand side contribute only when $m/(n-1) = 1, 3, 5, \ldots$ or $(m+1)/n = 1, 3, 5, \ldots$, respectively.

If only displacement-induced multipoles of lower order than the drive are of interest, i.e., $m < n$, then Eq. (6.10) gives a nonzero $O(\delta_x)$ contribution only for $m = n - 1$.

Equation (6.10) reproduces the free-space results derived above. For example, for a quadrupole drive and dipole response, $n = 2$, $m = 1$, the centered-pipe cross terms vanish and

$$H_{1,2}(p;\delta_x) = 2\delta_x \left[H_{1,1}(p) - H_{2,2}(p) \right]. \tag{6.11}$$

With $H_{j,j}(p) = 1/(1 + p\bar{\tau}_0/j)$, this reduces to Eq. (6.1). Similarly, extending the same construction to second order in δ_x for a sextupole drive gives

$$H_{1,3}(p;\delta_x) = 3\delta_x^2 \left[H_{1,1}(p) - 2H_{2,2}(p) + H_{3,3}(p) \right], \tag{6.12}$$

which reduces in free space to Eq. (6.2).

For the general case with finite magnet poles, Eq. (6.10) may be evaluated using the centered-pipe transfer functions derived in Sections 4–5. The vertical displacement case can be handled similarly to what was discussed after Eq. (6.3).

To conclude this section, we have derived the main result, Eq. (6.10), which allows one to calculate the $O(\delta_x)$ transfer functions induced by horizontal beam-pipe displacement from the corresponding centered-pipe transfer functions. The derivation relies on the assumption, not rigorously proven here, that for higher-order magnets the pole-boundary effects do not introduce additional $O(\delta_x)$ contributions beyond those captured by geometric feeddown. Therefore, Eq. (6.10) should be regarded as an ansatz constrained by geometric feeddown, by the known free-space displaced-pipe limits, and by the centered-pipe transfer functions derived earlier.

7 Comparison with Finite Element Method

In this section, a subset of the new analytical results presented above is validated against 2D frequency-domain finite-element simulations performed with COMSOL Multiphysics 6.3 [7]. For this purpose, we use a normal-conducting quadrupole as a representative example.

For clarity, only one quadrant of the quadrupole and beam pipe, both centered at the origin, is shown in Fig. 3. The simulations were conducted with the full magnet and beam pipe, although appropriate boundary conditions could also be used to simulate a fraction of the geometry. The magnet has a pole-tip radius $r_p = 33.97\,\mathrm{mm}$.

The pole-tip profile in the first quadrant is described by the hyperbola $x\,y = r_p^2/2$, where x and y are the horizontal and vertical coordinates, with the profile truncated to the range $12.51\,\text{mm} \le x \le 46.11\,\text{mm}$. The yoke material was assigned a relative permeability of 15000 (so the field intensity in the yoke is negligible) and a small but finite electrical conductivity of 0.25 S/m (to avoid running into numerical issues due to zero conductivity).

The magnet was excited with a spatially uniform current density across the coil cross-sections, resulting in 5.546 kA-turns per pole. The very small yoke conductivity, together with the imposed coil current density, ensures that the magnet itself does not contribute appreciably to the opposing eddy-current fields. The operational frequency was varied from 0.01 Hz to 10 kHz.

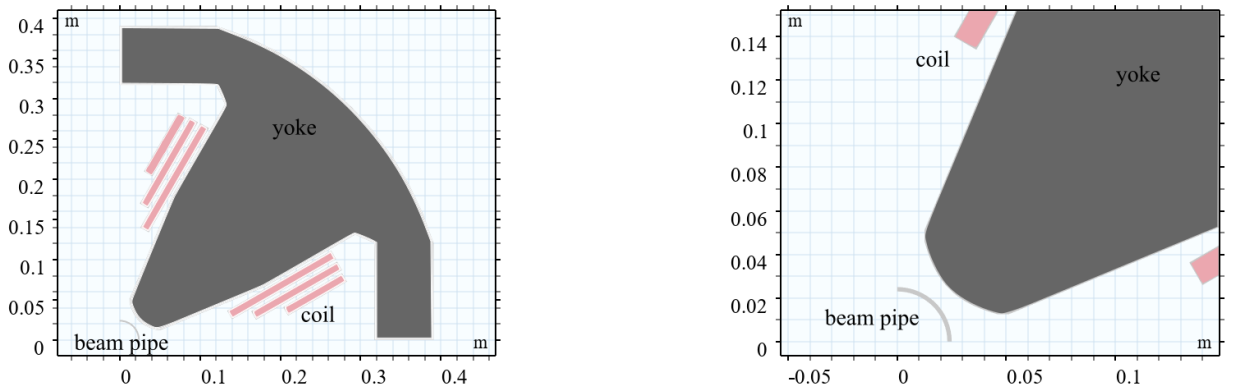

Figure 3: (left) One quadrant of the quadrupole and cylindrical beam pipe; (right) zoomed-in view.

The cylindrical beam pipe has an inner radius of 27.6 mm and a wall thickness of 0.7 mm, and is assigned an electrical conductivity of 2×10^7 S/m.

The flux density (field) magnitude in the region enclosed by the beam pipe for two excitation frequencies of 0.01 Hz and 1 kHz is shown in Fig. 4. The field magnitude decreases from 0.01 Hz to 1 kHz, demonstrating the shielding effect of the conductive beam pipe at higher frequency. Furthermore, the flux paths represented by solid gray lines in the figure show the four-fold symmetric nature of the fields, as expected.

In another study, the same beam pipe was displaced by 2 mm along the x-axis with the magnet still centered at the origin. The field magnitude and flux lines inside the beam pipe at an excitation frequency of 600 Hz are shown in Fig. 5. The flux lines are slightly shifted in the x-direction, indicating the presence of a dipole component in the field.

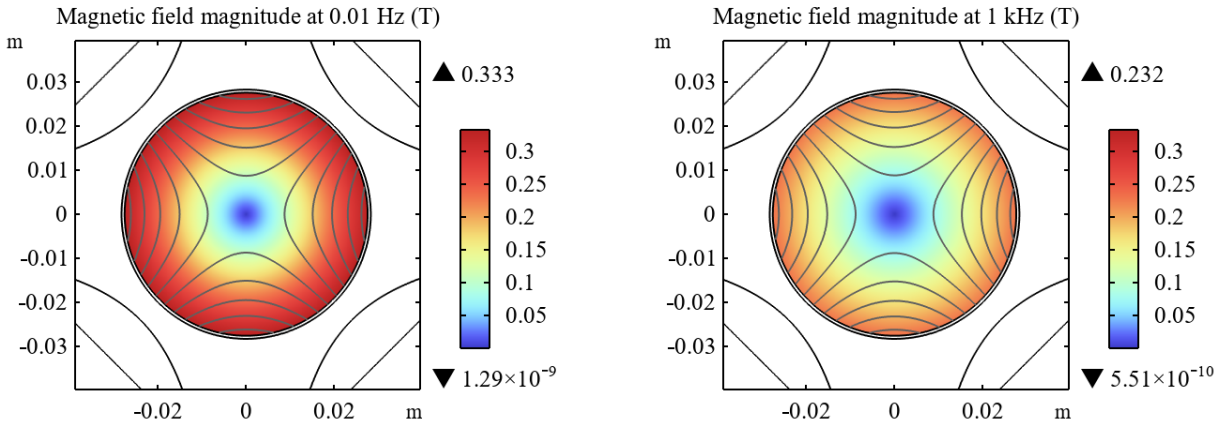

Figure 4: Field magnitude inside the beam pipe at excitation frequencies of 0.01 Hz and 1 kHz.

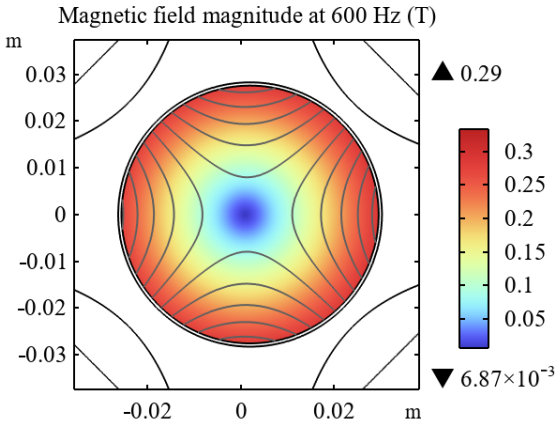

Figure 5: Flux density norm inside the circular beam pipe displaced horizontally by $\delta_x = 2\,\text{mm}$ at an excitation frequency of 600 Hz.

We next examine the frequency dependence of the field at the point $(11.5\,\text{mm}, 0)$, as well as the extracted multipole components, for the aligned and displaced-pipe cases.

Before doing so, we note that the FEM results considered here intentionally extend into the frequency range where the (electrically) thin-wall approximation assumed in this paper breaks down. We account for this effect in the comparisons below. Following Refs. [8, 9], the skin effect can be modeled by the transfer function

$$H_{\text{sk}}(p) = \prod_{k=1}^{N_{\text{max}}} \frac{|p_k|}{p - p_k}, \tag{7.1}$$

with unit DC gain, where

$$p_k = -k^2 \frac{\pi^2}{\mu_0 \sigma d^2}, \qquad k = 1, 2, 3, \ldots. \tag{7.2}$$

The pole values p_k correspond to frequencies for which $\delta_{\text{sk}}(\omega) = \sqrt{2}\, d/(\pi k)$. In contrast to the pole in Eq. (4.14), these poles do not depend on the driving multipole order or on the pipe radius, and they scale inversely with the square of the wall thickness. The total number of poles N_{max} should be chosen according to the highest frequency of interest and the desired accuracy.

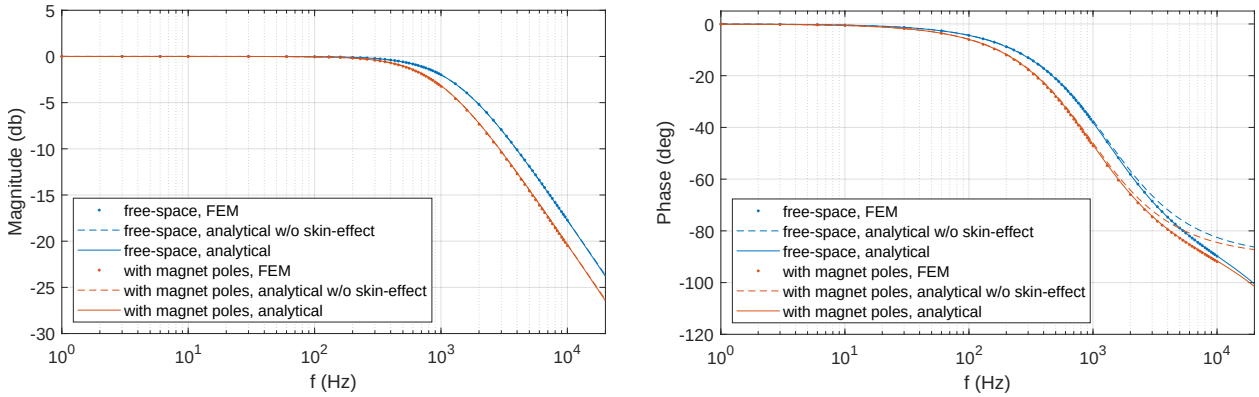

Figure 6: Self-response transfer functions from FEM and from Eq. (4.14).

Now we proceed with the comparison of FEM results with the analytical transfer functions derived in this paper, starting with the self-response field shown in Fig. 6. The figure shows very good agreement between the FEM results and the analytical self-response transfer function. At high frequency, the agreement is obtained

after multiplying the thin-wall result by the skin-effect factor $H_{\rm sk}(p)$; without this correction (dashed lines in Fig. 6), the phase lag is underestimated, while its effect on the amplitude is minor over this frequency range. In the remaining figures in this section, all analytical curves include the same skin-effect correction, i.e. they correspond to $H_{m,n}(p)H_{\rm sk}(p)$, with $N_{\max} = 20$.

We note that agreement of the transfer function also confirms the leading quadrupole term in the induced-field expansion, Eq. (3.18).

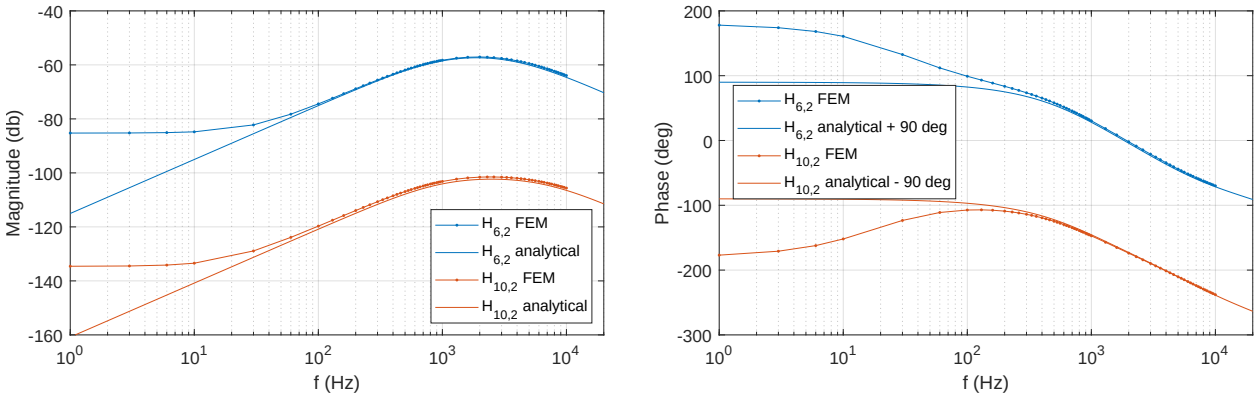

Figure 7: Cross-response transfer functions from FEM and from Eq. (5.6).

Next we consider the cross-responses. The two lowest-order quadrupole-driven cross-responses, $H_{6,2}$ and $H_{10,2}$, are shown in Fig. 7, which shows very good agreement in the high-frequency amplitude response. At low frequency, the FEM multipoles are dominated by residual static components, which obscure the dynamic cross-response. Agreement in the frequency-dependent part of the transfer functions also supports the corresponding cross-terms in the induced-field expansion, Eq. (3.18). The high-frequency phase agreement is also good after applying constant phase offsets of 90° for $H_{6,2}$ and −90° for $H_{10,2}$. These offsets most likely reflect a convention difference in the extraction or interpretation of complex FEM multipole phases, rather than a discrepancy in the predicted frequency dependence.

Finally, Fig. 8 shows the quadrupole-driven dipole response for a horizontally displaced beam pipe. The FEM and analytical phase responses agree well, while the overall amplitude differs by about 10%. Linearity with respect to the pipe offset was also confirmed in separate FEM simulations.

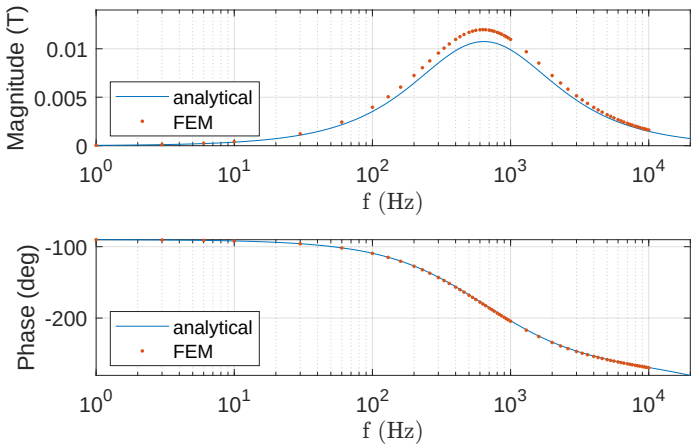

Figure 8: Quadrupole-driven dipole response for a beam pipe displaced horizontally by $\delta_x = 2$ mm: comparison of FEM results with Eq. (6.3).

In another simulation, the transfer functions were evaluated for a wider pole-tip region and were found to differ only marginally from those obtained with the original pole-tip truncation. This suggests that the

ideal-pole approximation used in the analytical derivation is not overly restrictive. Separately, although the FEM studies were performed with a small but finite yoke conductivity, the results are not expected to depend sensitively on this choice when the effective conductance of the beam-pipe wall is much larger than that of the yoke, as is typically the case for laminated magnets. In this limit, the opposing field is dominated by eddy currents in the beam pipe rather than by currents in the magnet yoke.

To summarize, comparison of the analytical results with detailed FEM calculations for a representative quadrupole magnet demonstrates very good agreement. Because the analytical construction follows the same structure for different drive multipoles, these comparisons provide useful validation of the approach for other common magnet types as well. In the next section, we apply this theory to make quantitative predictions for the major RCS magnets.

8 Results for the RCS

We start by introducing the relevant RCS parameters. The present design has a 316LN stainless-steel beam pipe with inner radius $a = 18.2\,\mathrm{mm}$ and wall thickness $d_{\mathrm{ss}} = 0.889\,\mathrm{mm}$. The inside of the beam pipe has a $30\,\mu$m-thick Cu coating. We take the conductivity values $\sigma_{\mathrm{ss}} = 1.35\times10^{6}\,(\Omega\cdot\mathrm{m})^{-1}$ and $\sigma_{\mathrm{Cu}} = 5.80\times10^{7}\,(\Omega\cdot\mathrm{m})^{-1}$. Because the induced wall currents run in parallel, the free-space dipole field penetration time constant is

$$\bar{\tau}_0 = \frac{1}{2}\mu_0\,(\sigma_{\mathrm{ss}}d_{\mathrm{ss}} + \sigma_{\mathrm{Cu}}d_{\mathrm{Cu}})\,a = 33.6\,\mu\mathrm{s}. \tag{8.1}$$

The pole-tip radii for the three major magnet types are: dipole — $r_p^{(d)} = 21\,\mathrm{mm}$ (one half of the full gap $g = 42\,\mathrm{mm}$); quadrupole and sextupole — $r_p^{(q)} = r_p^{(s)} = 20\,\mathrm{mm}$. From Eq. (4.15), the corresponding response time constants are $\tau_1 = 54.2\,\mu\mathrm{s}$, $\tau_2 = 26.2\,\mu\mathrm{s}$, and $\tau_3 = 16.3\,\mu\mathrm{s}$.

The exact time profile of the RCS beam-energy ramp is still being refined, but for the purposes of this paper it is sufficient to assume a perfectly linear ramp from $E_{\mathrm{min}} = 750\,\mathrm{MeV}$ to $E_{\mathrm{max}} = 18\,\mathrm{GeV}$ over $T_{\mathrm{ramp}} = 0.1\,\mathrm{s}$, corresponding to the dipole ramp rate $\dot{B}_0 = \dot{b}_1^{(e)} = 6.55\,\mathrm{T/s}$.

Assuming the lattice is maintained, all magnet fields must ramp in synchronism with the beam energy. Neglecting the small corrections from induced multipoles, this implies that $b_n^{(e)}(t) \propto E(t)$ for any n.

With the parameters defined above, Eq. (3.20), together with the multipole decomposition of Eq. (3.1) and the time constant from Eq. (8.1), allows one to calculate the induced m-pole coefficient, in units of $\mathrm{T/m}^{m-1}$, at any point of the ramp for any ramped n-pole magnet.

For beam-dynamics simulations, however, it is more convenient to normalize the induced multipole field at some reference radius r_{ref} to the nominal field of the ramped magnet [10]. Because the induced multipoles scale with the ramp rate while the normalization is proportional to the nominal magnet field, the normalized values are energy-dependent. Below we evaluate the normalized values at the minimum beam energy, where

$$\frac{\dot{b}_n^{(e)}}{(b_n^{(e)})_{\mathrm{min}}} = \frac{E_{\mathrm{max}}/E_{\mathrm{min}} - 1}{T_{\mathrm{ramp}}} = 230\,\mathrm{s}^{-1}, \qquad n = 1, 2, 3, \ldots, \tag{8.2}$$

where $(b_n^{(e)})_{\mathrm{min}}$ is the design multipole value at 750 MeV.

Applying this normalization, Table 1 lists the induced multipole fields for orders $m = 1, \ldots, 10$, in units of 10^{-4} of the nominal dipole, quadrupole, and sextupole fields, all evaluated at $r_{\mathrm{ref}} = 15\,\mathrm{mm}$. The centered-pipe entries were obtained from Eqs. (2.10), (3.18), and (3.19) by substituting the time constant from Eq. (8.1) and using Eq. (8.2) for normalization at the start of the ramp. Multipole orders forbidden by symmetry are listed as "0".

For each magnet type, the table also includes a row labeled $\delta_x = 1\,\mathrm{mm}$, showing the additional multipole contributions that would be generated by horizontal beam-pipe displacement from the magnet center; only terms linear in δ_x are retained. The dipole entries were obtained from Eq. (A.17), while the quadrupole and sextupole entries were obtained from the $O(p)$ asymptotic of Eq. (6.10).

The assumed displacement value $\delta_x = 1\,\mathrm{mm}$ is intentionally conservative; substantially smaller misalignments are expected in practice even without dedicated alignment procedures. Unlike the centered-pipe entries, the displaced-pipe multipoles should be scaled appropriately and assigned random signs in beam-dynamics simulations unless more specific information about the expected misalignment distribution

is available. The same entries also apply approximately to vertical displacement, except that the resulting multipoles should then be interpreted as skew.

The table entries correspond to the start of the energy up-ramp, where the adopted normalization gives their maximum values; see Eq. (8.2). At higher beam energy, the table entries should be scaled down by the ratio $E_{\min}/E(t)$.

Drive	Case	Induced normal multipole order m									
		1	2	3	4	5	6	7	8	9	10
Dipole	centered pipe	-125	0	12.0	0	-2.39	0	0.421	0	-0.0688	0
	$\delta_x = 1\,\mathrm{mm}$	0	-1.60	0	0.637	0	-0.168	0	0.0367	0	-0.00715
Quadrupole	centered pipe	0	-60.2	0	0	0	3.37	0	0	0	-0.418
	$\delta_x = 1\,\mathrm{mm}$	-4.32	0	0.800	0	-1.28	0	0.0281	0	0.246	0
Sextupole	centered pipe	0	0	-37.6	0	0	0	0	0	1.04	0
	$\delta_x = 1\,\mathrm{mm}$	0	-3.01	0	0	0	0.449	0	-0.555	0	-0.0557

Table 1: Induced multipole fields in units of 10^{-4} of the nominal field due to RCS ramped dipole, quadrupole, and sextupole magnets. The fields are evaluated at $r_{\mathrm{ref}} = 15\,\mathrm{mm}$ and at the start of the energy ramp, $E = E_{\min} = 750\,\mathrm{MeV}$. For the displaced-pipe rows, only $O(\delta_x)$ contributions are listed.

As expected, the table entries are dominated by the self-responses; for a given magnet type, the strongest cross-terms are at least one order of magnitude smaller. Even the self-responses remain relatively modest, reaching at most 1.25% of the main field for the dipole and decreasing with increasing drive-magnet order. When necessary, these can be readily compensated by adjusting the corresponding magnet power supplies.

For the displacement-induced multipoles, more detailed beam-dynamics studies are still required, but even for the conservative displacement value $\delta_x = 1\,\mathrm{mm}$, these effects appear small. For instance, the 4.32-unit magnitude of the quadrupole-induced dipole term is equivalent to a very minor dipole kick a beam would receive from the nominal quadrupole field when traveling on an orbit displaced by $\sim 6.5\,\mu\mathrm{m}$ from the quadrupole center.

Table 1 lists the multipole magnitudes obtained from the low-frequency $O(p)$ asymptotic of the transfer functions derived in Sections 4–6; the finite-frequency pole structure does not directly enter the table and affects only the transient evolution discussed below. We now briefly discuss the dynamical behavior implied by the full transfer functions, including the poles, as given by Eqs. (4.14), (5.6), and (6.10).

First, recall that the poles of the transfer functions are given by the inverse response times. For the present RCS parameters, the characteristic time constants for the three major magnet types were already given after Eq. (8.1): $\tau_1 = 54.2\,\mu\mathrm{s}$, $\tau_2 = 26.2\,\mu\mathrm{s}$, and $\tau_3 = 16.3\,\mu\mathrm{s}$. The corresponding characteristic frequencies, $f_i = (2\pi\tau_i)^{-1}$, are orders of magnitude higher than both the normalized ramp rate $230\,\mathrm{s}^{-1}$ and the 1 Hz RCS repetition frequency. Consequently, if the magnet fields in the absence of the beam pipe follow the design ramp, the corresponding fields inside the pipe will also follow the ramp very closely. For the self-response of a ramped n-pole magnet, the dominant dynamical effect is therefore simply a delay by the corresponding time constant τ_n.

The cross-response transfer functions, both for the centered pipe and for the displacement-induced terms, exhibit qualitatively different dynamics. For a perfectly linear ramp, the cross-response multipoles approach constant values after the transient has decayed, corresponding to the entries listed in Table 1. In this regime, the transfer-function poles no longer affect the response.

The high-frequency dynamics becomes most visible during transients, both for the self- and cross-response fields. For an idealized unit-slope linear ramp switched on at $t = 0$,

$$x(t) = t\,\Theta(t), \tag{8.3}$$

the self-response transfer function,

$$H_{n,n}(p) = \frac{1}{1 + p\tau_n}, \tag{8.4}$$

gives the time-domain response

$$y_n(t) = \left(t - \tau_n + \tau_n e^{-t/\tau_n}\right)\Theta(t), \tag{8.5}$$

whereas a representative cross-response transfer function,

$$H_{m\neq n,n}(p) = \frac{pK_{m,n}}{(1+p\tau_m)(1+p\tau_n)}, \tag{8.6}$$

gives

$$y_{m\neq n,n}(t) = K_{m,n}\left[1 - \frac{\tau_m e^{-t/\tau_m} - \tau_n e^{-t/\tau_n}}{\tau_m - \tau_n}\right]\Theta(t). \tag{8.7}$$

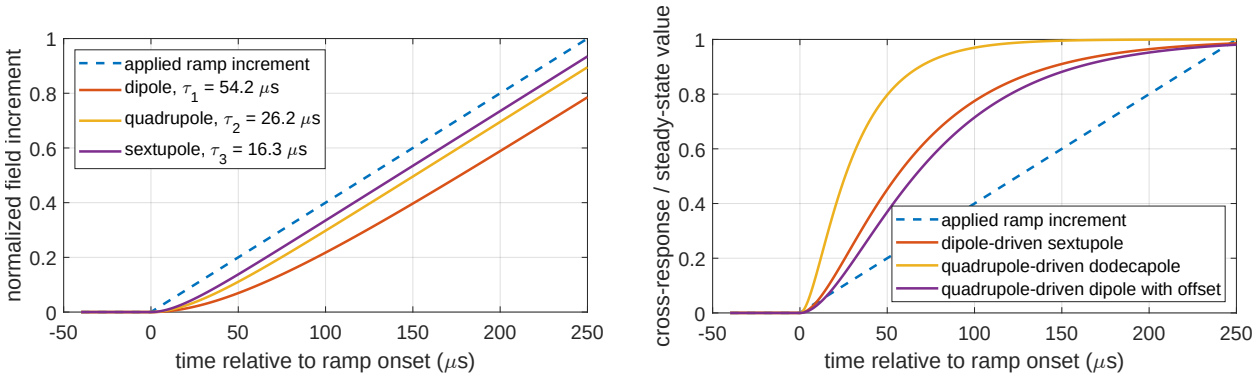

Figure 9: Time-domain evolution of the induced multipoles near the onset of an idealized linear ramp. Left: total self-response fields inside the pipe for dipole, quadrupole, and sextupole drive magnets. Right: representative centered- and displaced-pipe cross-response multipoles, normalized to their steady-state values.

These responses, evaluated using the RCS time constants, are illustrated in Fig. 9. For clarity, the transient responses in the figure are shown in normalized form.

Note that the instantaneous onset of the linear ramp shown in the figure is unrealistic; finite power-supply bandwidth, magnet inductance, and possibly an intentionally programmed slower ramp onset would smooth the transition. The figure nevertheless illustrates the important point that the self- and cross-response transfer functions exhibit qualitatively different dynamical behavior, both between self- and cross-responses and among different multipole combinations $\{m, n\}$. More importantly, it demonstrates the utility of the derived transfer functions for predicting transient multipole evolution beyond the low-frequency $O(p)$ approximation.

9 Summary

We investigated the generation of dynamic multipoles due to eddy currents induced by ramped normal-conducting magnets in circular beam pipes, and derived compact analytical expressions for the resulting magnetic fields and their dynamical response.

The induced multipole spectrum was analyzed in detail, leading to a selection rule whereby an n-pole drive generates only harmonics of orders n, $3n$, $5n$, and so on. Closed-form expressions for the corresponding induced multipole amplitudes were obtained, and it was shown that, for fixed drive order n, the cross-response amplitudes decrease rapidly with increasing generated multipole order.

We also investigated the dynamical aspects of multipole generation by deriving the corresponding frequency-domain transfer functions. The self-response from an n-pole drive is well described by a first-order transfer function with a time constant that is at most ~ 1.8 times larger than the free-space value $\bar{\tau}_0/n$. The symmetry-allowed cross-responses exhibit a zero at the origin and are well approximated by second-order transfer functions with two poles associated with the characteristic time scales of the participating modes.

This has an important practical consequence. Because the cross-responses vanish at zero frequency, the corresponding dynamic multipoles are additionally suppressed for sufficiently slow ramps. Nevertheless, they may still adversely affect the beam dynamics and therefore require careful evaluation.

Furthermore, although a cross-term multipole can in principle be partially compensated by another ramped magnet of the corresponding order, exact compensation over the full ramp is generally not possible

with a simple proportional correction waveform, because the cross-response and self-response transfer functions have qualitatively different dynamical behavior. If compensation is required, this finding favors passive compensation solutions; see, e.g., [11].

In addition to the symmetry-allowed cross-responses discussed above, we also considered the case in which symmetry itself is broken by a beam-pipe displacement δ from the magnet center. We showed that, in this case, higher-order magnets do generate induced dipole components. Their amplitudes scale as $O(\delta^{n-1})$, implying that a linear ($O(\delta)$) dipole term arises only for quadrupole drive. The corresponding approximate transfer functions were derived in closed form.

Detailed comparison of analytical results with FEM simulations (COMSOL Multiphysics) demonstrated very good agreement. While the analytical model assumes ideal pole geometries extending to infinity, the simulations confirm that truncation of the pole surfaces at realistic distances has only a minor effect. The comparison also indicates that finite yoke conductivity has little influence when the effective conductance of the beam-pipe wall dominates, as expected for laminated magnets. At higher frequencies, the skin effect across the beam-pipe wall becomes important; this can be incorporated by augmenting the thin-wall transfer functions with additional high-frequency poles.

The analytical results were applied to the RCS. For the present design, including the beam-pipe radius, wall thickness and material, magnet apertures, and ramp rate, we evaluated the dynamic multipoles and their evolution across the ramp, as summarized in Section 8. The self-responses, reaching up to ~ 125 units (normalized to the main field at $r_{\mathrm{ref}} = 15\,\mathrm{mm}$ at $E = 750\,\mathrm{MeV}$), are not expected to be problematic, as they can be compensated through power-supply control. More importantly, with the exception of the dipole-induced sextupole, all cross-term dynamic multipoles, including those induced by beam-pipe misalignment, are predicted to remain below ~ 5 units, comparable to typical tolerances for static multipoles. Preliminary beam-dynamics simulations [10] indicate that multipoles of this magnitude are acceptable for both beam-loss control and polarization preservation. The dipole-induced sextupole, estimated at 12 units, may require dedicated compensation.

The quantitative transfer functions obtained for the RCS multipoles, and summarized in Section 8, should be useful for the development of such a compensation system. Separately, they should also help establish high-frequency power-supply jitter tolerances and, at a later stage, support fine-tuning of individual magnet ramp profiles to synchronize the fields seen by the beam.

More generally, the analytical framework developed in this paper is directly applicable to other eddy-current-related problems in accelerators, such as power-supply ripple tolerances or magnet vibration tolerances in machines with circular vacuum chambers and normal-conducting magnets.

References

[1] S. Y. Lee, *A multipole expansion for the field of vacuum chamber eddy currents*, Nuclear Instruments and Methods in Physics Research A300, 1991, pg 151-158

[2] Y. Chen et al., *An expression for the eddy field in a circular vacuum chamber for HEPS booster dipole*, 2019, doi:10.48550/arXiv.1910.09781

[3] J. Tanabe, "Iron Dominated Electromagnets: Design, Fabrication, Assembly and Measurements," SLAC, Stanford, CA, USA, Rep. SLAC-R-754, May 2005. doi:10.1142/5823

[4] B. Podobedov, M. Blaskiewicz and H. Witte "Dynamic dipole kick due to a rippling sextupole", presented at the IPAC'25, Taipei, Taiwan, June 2025, paper THAN3.

[5] R.E. Shafer, "Eddy Currents, Dispersion Relations, and Transient Effects in Superconducting Magnets", Fermilab report TM-991 (1980)

[6] D. Rice, "Error Sources and Effects", in *Handbook of Accelerator Physics and Engineering*, A.W. Chao, M. Tigner, Eds, Singapore, 1998, World Scientific, pp.263-264

[7] https://www.comsol.com/comsol-multiphysics

[8] B. Podobedov, M. Blaskiewicz, "Eddy Current Shielding of the Magnetic Field Ripple in the EIC Electron Storage Ring Vacuum Chambers", BNL-224904-2023-TECH, EIC-ADD-TN-055, 2023

[9] B. Podobedov, H. Witte and M. Blaskiewicz, "Eddy current shielding of the magnetic field ripple in the EIC electron storage ring vacuum chambers", in *Proc. IPAC'24*, Nashville, TN, May 2024, pp. 246-249. doi:10.18429/JACoW-IPAC2024-MOPC77

[10] W. Bergan et al., "Status of the Rapid Cycling Synchrotron Optics", in *Proc. IPAC'26*, Deauville, France, May 2026, pp. 334-337. doi:10.18429/JACoW-IPAC2026-MOP1302

[11] Q. Wu et al., "Self-correction coil for RCS dipole in Electron Ion Collider", in *Proc. IPAC'24*, Nashville, TN, May 2024, pp. 1531-1533. doi:10.18429/JACoW-IPAC2024-TUPR49

A Compact expressions for the dipolar drive

We consider a thin-wall conducting circular pipe of radius a, wall thickness d, and conductivity σ, placed between two parallel high-permeability poles separated by the full gap g. The applied field is a time-dependent dipole drive with ramp rate $\dot{B}_0$.

We use the free-space dipole field penetration time constant, consistent with Eq. (4.2),

$$\bar{\tau}_0 = \frac{1}{2}\mu_0 \sigma d a, \tag{A.1}$$

and the normalized variables

$$\hat{z} = \frac{z}{a}, \qquad \hat{\zeta} = \frac{\zeta}{a}, \qquad \hat{g} = \frac{g}{a}. \tag{A.2}$$

The normalized source point $\hat{\zeta}$ is restricted to the circular wall, $|\hat{\zeta}| = 1$, whereas the normalized observation point $\hat{z}$ lies in the strip aperture, $|\Im(\hat{z})| < \hat{g}/2$.

We begin from the Dirichlet Green function for the strip

$$-\frac{\hat{g}}{2} < \Im(\hat{z}) < \frac{\hat{g}}{2}, \tag{A.3}$$

namely

$$G_S(\hat{z}, \hat{\zeta}) = \frac{1}{2\pi} \log \left| \frac{\cosh\left(\dfrac{\pi}{2\hat{g}}(\hat{z} - \hat{\zeta}^*)\right)}{\sinh\left(\dfrac{\pi}{2\hat{g}}(\hat{z} - \hat{\zeta})\right)} \right|. \tag{A.4}$$

By construction, $G_S(\hat{z}, \hat{\zeta})$ satisfies the Dirichlet boundary condition on the strip boundaries:

$$G_S\left(x \pm i\frac{\hat{g}}{2},\, e^{i\phi}\right) = 0, \qquad x, \phi \in \mathbb{R}.$$

Differentiation with respect to the observation point gives the corresponding complex kernel

$$K(\hat{z}, \hat{\zeta}) = \tanh\left(\frac{\pi}{2\hat{g}}(\hat{z} - \hat{\zeta}^*)\right) + \coth\left(\frac{\pi}{2\hat{g}}(\hat{z} - \hat{\zeta})\right). \tag{A.5}$$

Accordingly, the field produced at $\hat{z}$ by a filamentary current element dI located at $\hat{\zeta}$ is

$$dB(\hat{z}) = \frac{\mu_0}{4g}\left[\tanh\left(\frac{\pi}{2\hat{g}}(\hat{z} - \hat{\zeta}^*)\right) + \coth\left(\frac{\pi}{2\hat{g}}(\hat{z} - \hat{\zeta})\right)\right] dI. \tag{A.6}$$

The induced current is now placed on the circular wall,

$$\hat{\zeta} = e^{i\phi}. \tag{A.7}$$

For a dipolar drive, the wall current follows from Faraday's law as

$$dI = -\sigma d a^2 \dot{B}_0 \cos\phi \, d\phi, \tag{A.8}$$

provided one neglects the effect of the induced self-field on the wall-current distribution, as in Ref. [1].

Hence

$$B(\hat{z}) = -\frac{\mu_0 \sigma d a^2 \dot{B}_0}{4g} \int_0^{2\pi} \left[\tanh\left(\frac{\pi}{2\hat{g}}(\hat{z} - e^{-i\phi})\right) + \coth\left(\frac{\pi}{2\hat{g}}(\hat{z} - e^{i\phi})\right)\right] \cos\phi \, d\phi. \tag{A.9}$$

Introducing

$$\hat{\zeta} = e^{i\phi}, \qquad e^{-i\phi} = \frac{1}{\hat{\zeta}}, \qquad d\phi = \frac{d\hat{\zeta}}{i\hat{\zeta}}, \qquad \cos\phi = \frac{1}{2}\left(\hat{\zeta} + \frac{1}{\hat{\zeta}}\right), \tag{A.10}$$

the angular integral may be written as a contour integral on the unit circle, in the same spirit as [2]. Since

$$\cos\phi\, d\phi = \frac{1}{2}\left(\hat{\zeta} + \frac{1}{\hat{\zeta}}\right)\frac{d\hat{\zeta}}{i\hat{\zeta}} = \left(\frac{1}{2i} + \frac{1}{2i\hat{\zeta}^2}\right) d\hat{\zeta}, \tag{A.11}$$

we obtain

$$B(\hat{z}) = -\frac{\mu_0 \sigma da^2 \dot{B}_0}{4g} \oint_{|\hat{\zeta}|=1} \left[\tanh\left(\frac{\pi}{2\hat{g}}\left(\hat{z} - \frac{1}{\hat{\zeta}}\right)\right) + \coth\left(\frac{\pi}{2\hat{g}}(\hat{z} - \hat{\zeta})\right)\right]\left(\frac{1}{2i} + \frac{1}{2i\hat{\zeta}^2}\right) d\hat{\zeta}. \tag{A.12}$$

The first term is then converted to an ordinary meromorphic contour integral by the inversion

$$\hat{w} = \frac{1}{\hat{\zeta}}. \tag{A.13}$$

After renaming $\hat{w} \to \hat{\zeta}$, one obtains

$$B(\hat{z}) = -\frac{\mu_0 \sigma da^2 \dot{B}_0}{4g} \oint_{|\hat{\zeta}|=1} \left[\tanh\left(\frac{\pi}{2\hat{g}}(\hat{z} - \hat{\zeta})\right) + \coth\left(\frac{\pi}{2\hat{g}}(\hat{z} - \hat{\zeta})\right)\right]\left(\frac{1}{2i} + \frac{1}{2i\hat{\zeta}^2}\right) d\hat{\zeta}. \tag{A.14}$$

The integrand is now meromorphic in $\hat{\zeta}$, and the remaining evaluation is straightforward by residues. Carrying out this calculation for the interior region $|\hat{z}| < 1$ yields the final expression for the field inside the pipe

$$B(\hat{z}) = -\bar{\tau}_0 \dot{B}_0 \left(1 + \frac{1}{\hat{z}^2} - \frac{\pi^2}{\hat{g}^2}\operatorname{csch}^2\left(\frac{\pi\hat{z}}{\hat{g}}\right)\right), \qquad |\hat{z}| < 1. \tag{A.15}$$

For $|\hat{z}| > 1$, the pole at $\hat{\zeta} = \hat{z}$ lies outside the contour, so the coth-part contributes only the second-order pole at $\hat{\zeta} = 0$. The free-space terms are then absent, and one finds, outside the pipe,

$$B(\hat{z}) = -\bar{\tau}_0 \dot{B}_0 \left(-\frac{\pi^2}{\hat{g}^2}\operatorname{csch}^2\left(\frac{\pi\hat{z}}{\hat{g}}\right)\right), \qquad |\hat{z}| > 1, \qquad |\Im(\hat{z})| < \frac{\hat{g}}{2}. \tag{A.16}$$

For completeness, we include expressions for a pipe shifted from the magnet center. For a horizontal displacement, the result follows immediately from the two equations above by translational symmetry in the horizontal direction:

$$B(\hat{z}; \hat{\delta}_x) = B(\hat{z} - \hat{\delta}_x). \tag{A.17}$$

Near the center of the magnet, and for small pipe displacements, this results in $O(\hat{\delta}_x)$ feeddown terms to all multipoles prohibited by symmetry in the centered pipe case, as well as $O(\hat{\delta}_x^2)$ corrections to the allowed terms, as illustrated with the leading terms below,

$$B(\hat{z}; \hat{\delta}_x) = -\bar{\tau}_0 \dot{B}_0 \left[\left(1 + \frac{\pi^2}{3\hat{g}^2} - \frac{\pi^4 \hat{\delta}_x^2}{15\hat{g}^4} + O\left(\hat{\delta}_x^4\right)\right) + \hat{z}\left(\frac{2\pi^4 \hat{\delta}_x}{15\hat{g}^4} + O\left(\hat{\delta}_x^3\right)\right) + O\left(\hat{z}^2\right)\right]. \tag{A.18}$$

For a vertical displacement, however, the strip geometry no longer reduces to a simple translation of the centered solution, and a separate contour-integral evaluation is required. Writing the vertical offset as $i\hat{\delta}_y$, the corresponding interior field is

$$B(\hat{z}; \hat{\delta}_y) = -\bar{\tau}_0 \dot{B}_0 \left[1 + \frac{1}{(\hat{z} - i\hat{\delta}_y)^2} - \frac{\pi^2}{4\hat{g}^2}\left(\operatorname{csch}^2\left(\frac{\pi(\hat{z} - i\hat{\delta}_y)}{2\hat{g}}\right) - \operatorname{sech}^2\left(\frac{\pi(\hat{z} + i\hat{\delta}_y)}{2\hat{g}}\right)\right)\right], \tag{A.19}$$

which reduces to the centered result when $\hat{\delta}_y = 0$, since $\operatorname{csch}^2 u - \operatorname{sech}^2 u = 4\operatorname{csch}^2(2u)$.

For the corresponding exterior field, the first two terms in square brackets are omitted.

Expanding Eq. (A.19) near the origin

$$B(\hat{z}; \hat{\delta}_y) = -\bar{\tau}_0 \dot{B}_0 \left[\left(1 + \frac{\pi^2}{3\hat{g}^2} + \frac{\pi^4 \hat{\delta}_y^2}{15\hat{g}^4} + O\left(\hat{\delta}_y^3\right)\right) + \hat{z}\left(-\frac{7\left(i\pi^4\right)\hat{\delta}_y}{60\hat{g}^4} + O\left(\hat{\delta}_y^3\right)\right) + O\left(\hat{z}^2\right)\right], \tag{A.20}$$

shows that small vertical offset results in the induced skew quadrupole linear with the offset, as well as a quadratic correction to the normal induced dipole. Comparing Eqs. (A.18) and (A.20) shows that $O(\hat{\delta}_x)$ and $O(\hat{\delta}_y)$ feeddown terms are not completely symmetric, although the magnitudes of the coefficients are close. For higher powers of $\hat{z}$ (not shown), the corresponding horizontal- and vertical-displacement coefficients rapidly converge in magnitude.